




Review

Diffusion in Nanoporous Materials: Novel Insights by Combining MAS and PFG NMR

Jörg Kärger * , Dieter Freude  and Jürgen Haase 

Fakultät für Physik und Geowissenschaften, Universität Leipzig, Linnéstraße 5, 04103 Leipzig, Germany; Freude@uni-leipzig.de (D.F.); j.haase@physik.uni-leipzig.de (J.H.)

* Correspondence: kaerger@uni-leipzig.de; Tel.: +49-341-973-2502

Received: 6 August 2018; Accepted: 21 August 2018; Published: 1 September 2018



Abstract: Pulsed field gradient (PFG) nuclear magnetic resonance (NMR) allows recording of molecular diffusion paths (notably, the probability distribution of molecular displacements over typically micrometers, covered during an observation time of typically milliseconds) and has thus proven to serve as a most versatile means for the in-depth study of mass transfer in complex materials. This is particularly true with nanoporous host materials, where PFG NMR enabled the first direct measurement of intracrystalline diffusivities of guest molecules. Spatial resolution, i.e., the minimum diffusion path length experimentally observable, is limited by the time interval over which the pulsed field gradients may be applied. In “conventional” PFG NMR measurements, this time interval is determined by a characteristic quantity of the host-guest system under study, the so-called transverse nuclear magnetic relaxation time. This leads, notably when considering systems with low molecular mobilities, to severe restrictions in the applicability of PFG NMR. These restrictions may partially be released by performing PFG NMR measurements in combination with “magic-angle spinning” (MAS) of the NMR sample tube. The present review introduces the fundamentals of this technique and illustrates, via a number of recent cases, the gain in information thus attainable. Examples include diffusion measurements with nanoporous host-guest systems of low intrinsic mobility and selective diffusion measurement in multicomponent systems.

Keywords: NMR; PFG; MAS; diffusion; adsorption; hierarchical host materials

1. Introduction

Diffusion, i.e., the irregular movement of the elements of a given entity in nature, technology, or society, is an essentially omnipresent phenomenon [1] and may often be found to decide about the performance of the systems under study. This is, in particular, true for nanoporous host-guest materials where the performance, i.e., the gain in value-added products by matter upgrading via separation [2,3] or conversion [4,5], can never be faster than allowed by the rate of mass transfer [6–8]. Measurement of the rate of mass transfer in nanoporous materials, however, is complicated by the small size of the individual crystallites (or particles). It was only with the introduction of the pulsed field gradient (PFG) technique of nuclear magnetic resonance (NMR) that the direct measurement of intracrystalline diffusivities has become possible [9–11]. The information provided by PFG NMR in its broadest significance is the probability distribution of molecular displacements, referred to as the mean propagator [12–14]. It does, thus, notably, include the intracrystalline self-diffusivity D , resulting via the Einstein relation [8,15] from the time dependence of the mean square displacement,

$$\langle r^2(t) \rangle = 6Dt \quad (1)$$

during the observation time t , i.e., from the squared width (the variance) of the propagator. As a prerequisite of such measurement, the root-mean-square displacement must be much smaller than the size of the crystals under study so that, during the observation time (typically in the range of milliseconds), the diffusion paths (typically of the order of micrometers) may be implied to remain unaffected by any significant interference with the crystal surface. The displacements must, simultaneously, be large enough for giving rise to a diffusion-related attenuation of the NMR signal.

The first requirement is seen to be easily fulfilled as soon as the material under study is accessible with sufficiently large crystal sizes. Accessibility of sufficiently large zeolite crystallites [16] did thus prove to be a very fortunate pre-condition for performance of the very first PFG NMR measurements with zeolites [9,17]. In view of Equation (1), the second pre-condition might also appear to be easily obeyed by simply choosing sufficiently long observation times. PFG NMR observation times, however, cannot be chosen to be arbitrarily large. They are rather limited by the influence of transverse nuclear magnetic relaxation which, via Equation (1), also sets a limit on the mean molecular displacements, depending on the given diffusivities (which, in PFG NMR studies, typically cover a range from $10^{-14} \text{ m}^2 \text{ s}^{-1}$ to $10^{-8} \text{ m}^2 \text{ s}^{-1}$). The minimum displacement still observable by PFG NMR is proportional to the amplitude of the field gradient pulses and to the duration over which the field gradients may be applied. While the maximum gradient amplitude is a key parameter of the given device, the maximum width of the field gradients is determined by a characteristic quantity of the system, namely by the transverse nuclear magnetic relaxation time of the molecules under study. The here-important value T_2^{echo} can be obtained by measurements of the Hahn echo decay in dependence on the pulse distance between the two radio frequency pulses. Notably, in systems of low mobility, where gradients with particularly large widths were needed for recording particularly small displacements, rapid transverse nuclear magnetic relaxation prohibits, as a rule, their application.

Novel access towards the application of larger field gradient pulse widths has been provided by the recent combination of PFG NMR measurement with the application of magic-angle spinning (MAS) [18–22]. Enhancement of the transverse relaxation time $T_2^{\text{MAS echo}}$ with respect to T_2^{echo} upon MAS allows longer gradient pulse widths and is accompanied by a reduction in NMR line width so that MAS PFG NMR offers, as a second advantage, distinction between different components and, hence, the option of selective diffusion measurement in mixtures where conventional PFG NMR would fail. The advantages of MAS PFG NMR are purchased, however, with a decrease in the amplitude of the field gradient pulses applied, as a simple consequence of the reduction in space available for the PFG NMR coils, brought about by the presence of the MAS NMR rotor. Application of MAS PFG NMR should always be accompanied, therefore, by thoughtful balancing of pros and cons.

We are introducing this novel field of diffusion measurement with a short summary of the experimental procedure and the physical background in Section 2. Showcases of the application of MAS PFG NMR are presented in Section 3. They include selective diffusion measurements with mixtures of hydrocarbons in microporous materials, notably zeolites and metal–organic frameworks (MOFs) (Section 3.1) and in mesoporous silica gel (Section 3.2). Section 3.3 deals with the application of MAS PFG NMR for investigating the diffusion properties of nematic liquid crystals under confinement. Section 3.4 illustrates the potential of MAS PFG NMR for tracing and characterizing the diffusion pathways of water molecules in zeolite X. In Section 3.5, the self-diffusion coefficients from MAS PFG NMR are compared with tracer diffusion coefficients which were derived from impedance spectroscopy by the Nernst-Einstein equation and provide a model for proton mobility in functionalized mesoporous materials. The paper concludes with a summary of pros and cons and a view into promising future applications.

2. Experimental Procedure

Before describing the measurement procedure commonly used in MAS PFG NMR in more detail, we are going to briefly recollect the measuring principle of PFG NMR in its most straightforward variant (for more extensive presentations see, e.g., [8,14,23,24]). Its fundamentals can be easily

rationalized within the frame of the classical interpretation of nuclear magnetism which is based on the understanding that a nuclear spin (in the cases here considered in general protons, i.e., the nuclei of hydrogen, ^1H) possesses both a magnetic and a mechanic momentum. Nuclear spins perform, therefore, within a magnetic field, a precessional motion (i.e., they rotate around the direction of the magnetic field) with an angular frequency vector of the Larmor frequency

$$\omega_L = -\gamma B_0 \quad (2)$$

where the magnetic induction, B_0 , stands for the intensity of the external magnetic field in the z direction, and γ denotes the gyromagnetic ratio. Chemical shift reference materials of all NMR isotopes were fixed by the IUPAC (International Union of Pure and Applied Chemistry) convention in 2001 [25]. In PFG NMR, a properly chosen pulse sequence gives rise to a preferential orientation of the individual nuclear magnetic moments with a component perpendicular to the direction of the constant magnetic field. Just as each individual spins, their vector sum also performs a rotational motion about the direction of the magnetic field. This rotating (nuclear) magnetization induces a voltage in a transverse coil surrounding the sample which is recorded as the NMR signal.

Diffusion measurement by PFG NMR is based on the application of a strong additional z -gradient field $B_{\text{add}} = gz$, superimposed upon the constant external one over a short time interval δ . The thus-created spreading in the local magnetic field and, hence, via Equation (2), in the rotational frequencies of the local magnetizations gives rise to a spreading in their orientation and, hence, to the decrease in their vector sum, i.e., in total magnetization, with the NMR signal fading away. With a second, identical field gradient pulse, properly placed within the PFG NMR pulse program after a certain time interval (in the PFG NMR literature generally referred to as the observation/diffusion time Δ), one is able to counteract this process by creating a phase shift in exactly the opposite direction. Correspondingly, all phase shifts are eliminated by this second field gradient pulse if all molecules have kept their positions. Molecules, however, which have been shifted (over a distance z) in the field gradient direction undergo a phase shift $\gamma gz\delta$ and contribute, correspondingly, with only the cosine of this shift to the overall signal. The attenuation of the NMR signal intensity $S(m,t)$ under the influence of diffusion and the field gradients applied is thus easily seen to be given by the relation [10,12]

$$S(m,t) = S(0,t) \int_{-\infty}^{\infty} \cos(mz)P(z,t)dz, \quad (3)$$

where $m = \gamma g\delta$, with gradient intensity g and gradient pulse duration δ , has been introduced as a measure of the intensity of the field gradient pulses and t stands for the observation time, Δ , of the PFG NMR experiment. $P(z,t)$ is the mean propagator [12,26], referred to already in the introduction. It denotes the probability (density) that, during the observation time t , an arbitrarily selected molecule within the sample (contributing to the observed NMR signal) is shifted over a distance z in the direction of the applied field gradient. With the notation of Equation (3) it has, further on, been implied that molecular displacements occurring during the field gradient pulses are negligibly small in comparison with the displacements in the interval between the two gradient pulses. For normal diffusion in an infinitely extended medium, the mean propagator is easily found to be given by a Gaussian [8,15,27]

$$P(z,t) = (4\pi Dt)^{-1/2} \exp\left[-z^2/(4Dt)\right] \quad (4)$$

with D denoting the self-diffusivity. Inserting Equation (4) into Equation (3) yields

$$\psi = \frac{S(m,t)}{S(0,t)} = \exp\left(-\gamma^2 g^2 \delta^2 Dt\right) = \exp\left(-\frac{1}{6}\gamma^2 g^2 \delta^2 \langle r^2(t) \rangle\right) \quad (5)$$

where, with the latter equality, we have made use of Equation (1). For the PFG NMR signal attenuation we have, moreover, introduced the common notation ψ . The time and space scales relevant for

Equations (3) and (5) are typically of the order of milliseconds and micrometers. Measurement of particularly small displacements $\langle r^2(t) \rangle^{1/2}$ is seen to require particularly large pulsed field gradient intensities $g\delta$. Since the amplitude g of the field gradient pulses is limited by the constructional details of the PFG NMR probe, the maximum value of the pulse width δ decides the minimum displacements accessible by PFG NMR. In conventional PFG NMR, however, the pulse width δ is limited by the relaxation time T_2^{echo} of transverse magnetization. It is this component of nuclear magnetization from which, with Equation (2), the space-dependent phase spreading and, as a consequence, signal attenuation by molecular displacements has been shown to originate. This decay in transverse magnetization, however, is notably slowed down for samples sufficiently quickly rotating, with a spinning axis oriented under an angle of $\theta_{\text{mas}} = \arccos 3^{-1/2} \approx 54.7^\circ$ with reference to the external magnetic field.

This option of enhancing the time interval over which magnetic field gradients may be applied is exploited in MAS PFG NMR [19,20,22,28–30]. Figure 1 introduces the experimental arrangement and the pulse program used in the measurement.

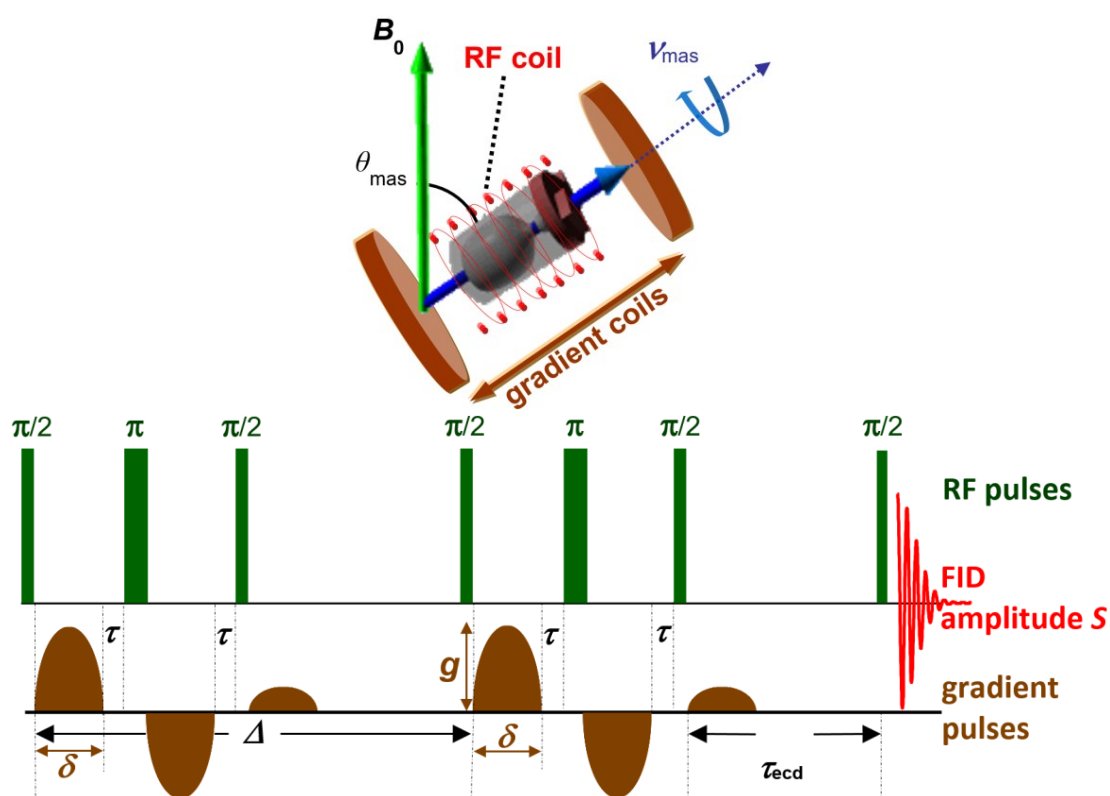


Figure 1. A representation of the MAS (magic angle spinning) design with two gradient coils on the top and on the bottom of the MAS stator in a high-resolution wide-bore MAS NMR (nuclear magnetic resonance) probe at the top. Radio frequency (RF) and gradient pulse scheme of the MAS pulsed field gradient (PFG) NMR experiment is shown below. Parameters are diffusion time Δ and gradient pulse width δ . The gradient pulse amplitude is denoted as g , the eddy current delay as τ_{eed} , and the inter-gradient delay as τ . Two weak spoiler gradient pulses average undesirable coherences [20].

The arrangement of the NMR sample tube containing the nanoporous host material and the guest molecules is shown in the top of Figure 1. We note the “magic-angle” of about 54.7° between the spinning axis and the direction of the magnetic field. The direction of the spinning axis coincides with that of the field gradient so that the local magnetic field within the sample (and thus, with Equation (2), the local rate of rotational motion) remains unaffected by sample rotation. Molecular displacements

recorded by analyzing the signal attenuation under the influence of the gradient pulses may thus indeed be attributed to diffusion phenomena within the sample.

The pulse sequence shown in the bottom of Figure 1 includes a number of differences in comparison with the basic version of PFG NMR as initially introduced. We note that the field gradient pulses are of sinusoidal, rather than of rectangular shape. This facilitates switching of the current used for generation of the field gradients and diminishes the occurrence of eddy currents in the radio frequency (RF) coil, which might interfere with the NMR signal. Serving the same purpose, pairs of opposing field gradient pulses (generated by opposing currents) rather than single ones are applied. The RF “ π ” pulse appearing in between such a pair gives rise to a rotation of all spins by 180° so that the “effective” gradients acting on the spins are identical. The initial $\pi/2$ pulse is recognized as the starting point of the experiment when the equilibrium magnetization showing in the direction of the constant magnetic field B_0 is turned, by 90° , into the plane perpendicular to B_0 . We note that with the last $\pi/2$ pulse, magnetization is once again turned into the plane perpendicular to B_0 , giving rise to the NMR signal S (the initial value of the “free induction decay”). Signal attenuation for the pulse sequence shown in Figure 1 is given by the relation [20]

$$\psi = \frac{S(m, t)}{S(0, t)} = \exp\left(-\frac{16}{\pi^2} \gamma^2 g^2 \delta^2 D t\right) = \exp\left(-\frac{8}{3\pi^2} \gamma^2 g^2 \delta^2 \langle r^2(t) \rangle\right). \quad (6)$$

The time t also includes, in addition to Δ , corrections due to finite pulse widths. The meaning of the gradient pulse width δ (see Figure 1) is for sine-shaped alternating pulses and, hence, changed in comparison with the basic experiment with two rectangular field gradient pulses, giving rise to a slightly different pre-factor in the exponents in Equations (5) and (6).

By combining the application of field gradient pulses with fast sample spinning, the time interval δ over which magnetic field gradients may be applied can be notably enhanced, in some cases over several orders of magnitude. In this way, molecular displacements which are too small to be observable by conventional PFG NMR become accessible by direct observation. This possibility is provided by the dramatic enhancement of the transverse nuclear magnetic relaxation time under the conditions of magic-angle spinning, $T_2^{\text{MAS echo}}$, in comparison with T_2^{echo} , the value observed without MAS. Enhancement of the transverse nuclear magnetic relaxation time leads, simultaneously, to decreasing line widths so that different chemical compounds can be distinguished on the basis of their NMR spectra.

Magnetic field gradient pulses in conventional PFG NMR can today be operated with values above 20 T/m. Schlayer et al. [31], e.g., achieved a value of 37 T/m with a 100 A power supply. The design with two gradient coils on the top and on the bottom of the MAS stator of a Bruker probe reaches about 0.5 T/m with a 10 A power supply. Narrow-bore MAS designs without gradient coils which are located in the imaging gradient tube of a wide-bore magnet achieve, with three 60 A power supplies, about 2 T/m.

In spite of these low gradient intensities, application of MAS PFG NMR proves to be the method of choice in quite a number of situations including, notably, selective multicomponent diffusion measurement in such systems where the spectra recorded by conventional PFG NMR fail in providing the resolution necessary for differentiating between various guest components. The subsequent section is going to highlight these advantages with a number of show cases.

While, as a matter of course, gravity in a non-rotating sample coincides with that in our natural surroundings, it becomes some hundred-thousand-fold higher in a rotating sample at 10 kHz. It is worthwhile mentioning, therefore, that molecular microdynamics within the spinning sample tubes remains essentially unaffected by this high rotational frequency, since intermolecular forces are much larger than the influence of gravity. Thus it could be observed by ^{11}B MAS NMR spectroscopy [32] that the parameters of crystallization upon super-gravity downgrade by less than one order of magnitude. For adsorption or catalysis in porous materials, we do not know of any report about the influence of supergravity by MAS. In cases with availability of both PFG NMR and MAS PFG NMR results,

like for *n*-alkanes adsorbed in silicalite-1 [33], no significant difference could be found. It is true, however, that operation with a high-velocity gas stream for ensuring high-speed sample rotation up to tens of kHz gives rise to a temperature difference between the “rotor” (with the fused sample tube) and the bearing air (whose temperature is accessible to direct measurement). This requires a separate temperature calibration. It is commonly based on measurement of the ^{207}Pb MAS NMR signal of $\text{Pb}(\text{NO}_3)_2$ within the sample tube whose temperature dependence is well known [34–36]. Temperatures within rotor and sample were thus found to exceed the temperature in the stator by about 10 K for a 4 mm rotor spinning at 10 kHz, with the option of a slight temperature gradient versus the sample.

3. Diffusion Measurement by MAS PFG NMR

3.1. Mixture Diffusion in Microporous Materials

Figure 2 introduces the potential of MAS PFG NMR for investigating mixture diffusion with a particularly simple case. On considering a 1:1 molar mixture of ethene and ethane (each with a loading of two molecules per cage), one benefits from the exceptional situation that in either compound all hydrogens are chemically equivalent. They are, therefore, “shielded” by identical “electronic clouds” so that the shift in the local field (and, hence, via Equation (2), in the frequency of the NMR signal) in comparison with the externally applied one is identical. Both molecules therefore give rise to different signals. These two lines are, as to be seen on the left in Figure 2, well separated from each other so that one may easily record the attenuation of the intensity (that is, the area under the line (the “band”)) of each of them as a function of the gradient intensity. The logarithmic representation of this attenuation as a function of the squared gradient intensity in Figure 2 is found to be in nice agreement with the expected behavior as predicted by Equation (6). The resulting diffusivities are $1.21 \times 10^{-10} \text{ m}^2 \text{ s}^{-1}$ for ethene and $0.27 \times 10^{-10} \text{ m}^2 \text{ s}^{-1}$ for ethane.

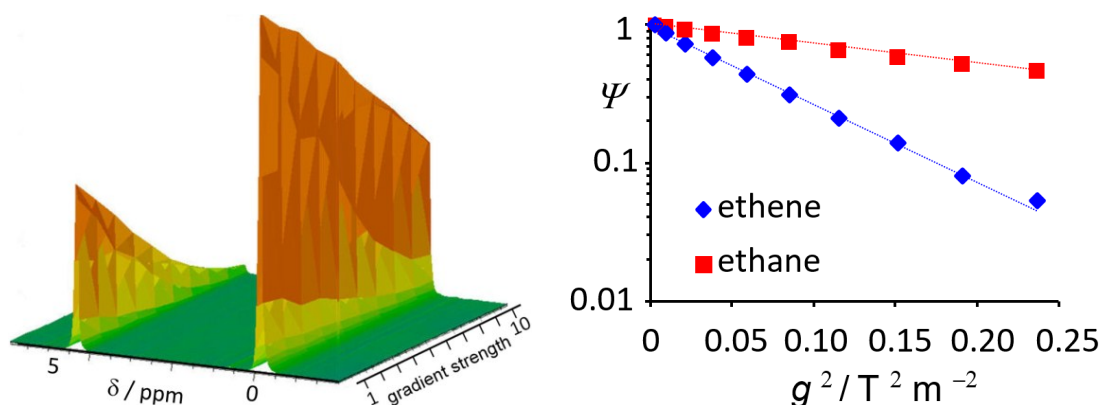


Figure 2. On the left is a 2D presentation of the ^1H MAS PFG NMR signal decay with 10 steps from 0.05 to 0.5 T/m linearly increasing strength of the gradient pulses for a ZIF-8 sample loaded with two ethene and two ethane molecules per cavity measured at 363 K. The logarithmic decay as a function of the squared gradient magnitude is presented on the right [37].

Given the similarity in the molecular critical diameters (0.39 nm for ethene, 0.40 nm for ethane [38]) the substantial difference in the diffusivities is quite remarkable. It can, however, be associated with the fact that these diameters significantly exceed the diameter of about 0.34 nm of the “windows” between adjacent cages as determined by X-ray diffraction analysis [39]. Under such conditions, already minor changes in size of the guest molecules may indeed be expected to dramatically affect their diffusion properties. With “windows” smaller than the diffusing molecules, diffusion is only possible in sufficiently flexible host lattices. This, however, is among the main features of metal-organic frameworks (MOFs) quite in general and of ZIF-8 as one of its representatives in particular. High

resistivity and durability in comparison with other MOFs have made it an interesting topic of research [40,41]. Studies include extensive diffusion measurements based on microimaging via IR microscopy [42]. For ethene and ethane the thus-obtained results were found to be in nice agreement with the diffusivities obtained by MAS PFG NMR [38]. IR microimaging did, moreover, allow an extension of the measurements to longer chains and, thus, to lower diffusivities.

As a common feature of all these systems, molecular jumps through the windows between adjacent cages can be considered as the rate-controlling step in molecular propagation. By adopting classical transition state theory (TST, with the jump through the window as the “activated state” [43–45]), the concentration dependence of the jump rates in such systems and, hence, of the self-diffusivity may be shown to be proportional to the ratio $p(c)/c$ between the guest pressure in the surrounding atmosphere and the guest concentration under equilibrium [46]. This prediction has been confirmed in [46] with the diffusivity data obtained by recording molecular uptake and release of a large spectrum of guest molecules (ethene, ethane, propene, propane, methanol, and ethanol) on ZIF-8 [38]. Such measurements benefit from the fact that in uptake and release measurements there exists, essentially, no lower limit on the accessible diffusivities. Moreover, pressure variation in the surrounding atmosphere allows a straightforward and most accurate variation of the guest concentration. Such a possibility does not exist in MAS PFG NMR measurements. Although also here, in the course of sample preparation, very accurate guest concentrations may be attained, these concentrations tend to decrease during sample fusing, as the indispensable last step in sample preparation for enabling sample spinning during the measurement. Although it is true that guest concentrations may be determined quite accurately from their signal intensity, there is an unavoidable (and, with factors up to 2, quite substantial) scattering in the attained concentrations, which significantly complicates any systematic investigation of concentration dependencies. The view of TST on molecular propagation helps in rationalizing why the diffusivities of the individual molecules under multicomponent adsorption (as considered in the MAS PFG NMR measurements) and single-component adsorption (microimaging) do essentially coincide since the jump rate from cage to cage can be expected to be only marginally affected by the composition of the cage population.

A totally different microdynamic situation is reflected by the self-diffusivity data shown in Figure 3 for a series of *n*-alkanes and *n*-alkenes in zeolite silicalite-1 [33]. Pore diameters in silicalite-1 are between 0.51 nm and 0.56 nm and thus notably exceed the critical diameters of the guest molecules considered. The slight difference in the critical diameters of alkenes (ethene) and alkanes (ethane), which has given rise to a substantial difference of the diffusivities in narrow-pore ZIF-8, is now of essentially no influence anymore. Diffusivities of *n*-alkanes and *n*-alkenes in silicalite-1 are found to essentially coincide. For a given number of guest molecules we note, correspondingly, that the diffusivity remains essentially the same under the conditions of single-component and mixture adsorption.

It is shown in Figure 3 that the diffusivities decrease with increasing chain length, also following the pattern well known from previous PFG NMR studies [47–49]. Increase in chain length by one CH₂ element is found to cause a decrease in the diffusivity by a factor of about 0.4.

The measurements reported in [33] did also agree with previous PFG NMR studies [47–49] in the finding (not shown in Figure 3) that the diffusivity monotonically decreases with increasing loading. This behavior also notably deviates from the patterns observed with ZIF-8 where the diffusivities could be found to both decrease and increase with loading [46]. The monotonic decay with increasing loading is easily attributed to the increase in friction between the guest molecules in the more open pore structure. One may observe a remarkably uniform dependence following a relation $d \lg D/d L = -0.55 \pm 0.10$ [33] where L is a measure of the loading, normalized with the understanding that $L = 1$ refers to one molecule per channel intersection (or to four molecules per unit cell).

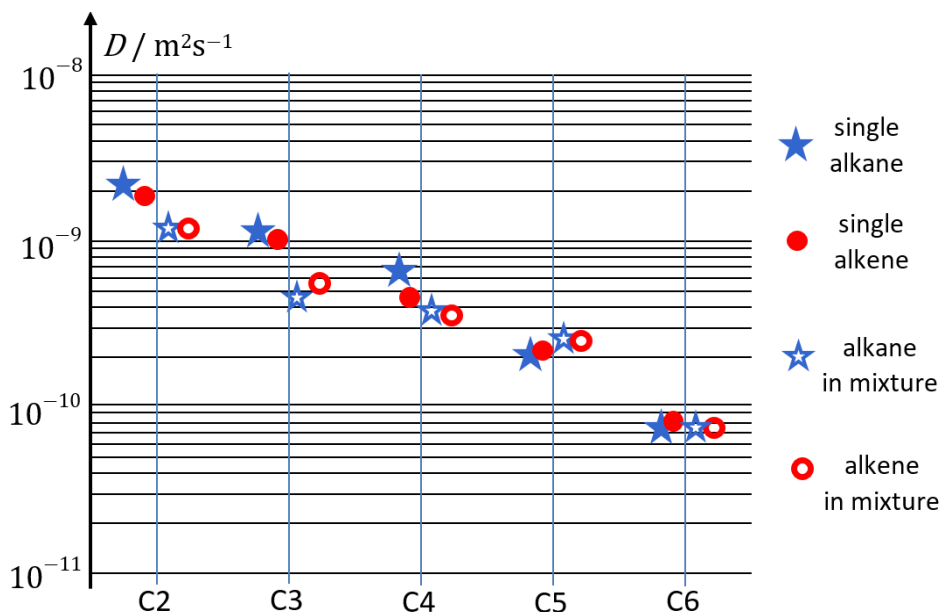


Figure 3. Self-diffusion coefficients of *n*-alkanes, alkenes, and one-to-one alkane/alkene mixtures in silicalite-1 at the temperature of 313 K for a total loading of about one molecule per crossing or less [33].

3.2. Complex Formation in Acetone–*n*-Alkane Mixtures Revealed via MAS PFG NMR

The properties of *n*-alkanes are known to exhibit minor deviations from a strict monotonic variation with increasing chain lengths. These deviations appear, e.g., in an oscillation in the melting points [50], attributed to an oscillation in the intermolecular forces, with stronger ones for the even-numbered *n*-alkanes [51,52]. This oscillation in interaction has been expected to be as well observable in complex formation with other compounds, notably including ketones [53]. Figure 4 illustrates the favorable conditions offered by MAS PFG NMR for selective diffusion studies with acetone–*n*-alkane mixtures.

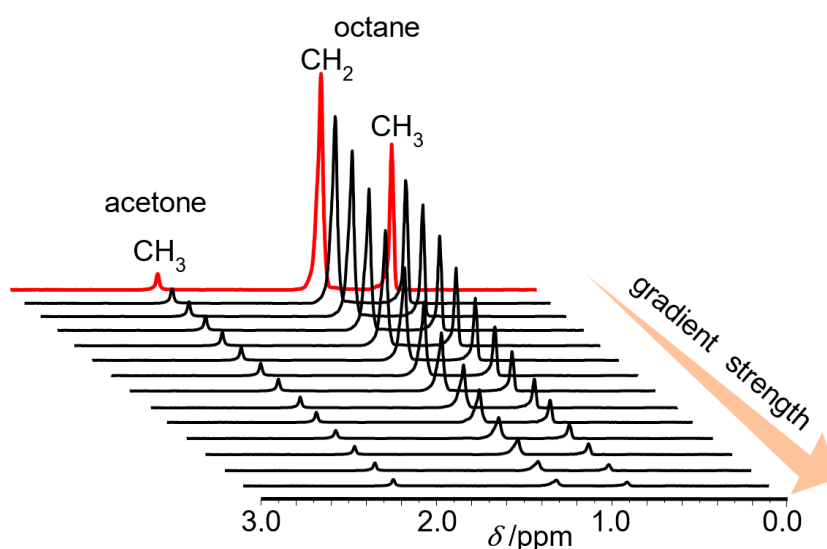


Figure 4. Stack plot of ^1H MAS PFG NMR spectra of a 1:10 acetone–*n*-octane mixture adsorbed in porous glass [54].

Figure 5 provides a comparison of the diffusivities of acetone and of various *n*-alkanes (from *n*-hexane up to *n*-nonane) in their binary mixture within a narrow-pore silica gel. In Figure 5a, the mean

pore size is about 4 nm and the acetone/*n*-alkane molar ratio is 1:10. Figure 5b shows the results within a larger-pore silica gel with a mean pore size of about 10 nm and an acetone/*n*-alkane molar ratio of 1:20.

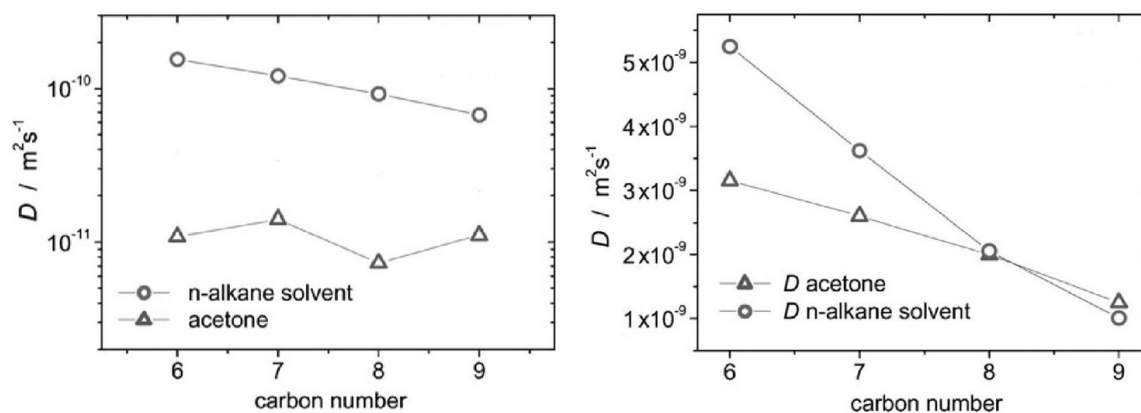


Figure 5. Diffusivities of the two components of the acetone–*n*-alkane mixtures in the narrow-pore silica gel on the left and in the large-pore silica gel on the right in dependence on the *n*-alkane chain length [54].

As a main difference between the two representations, acetone diffusivities in narrow-pore silica gel are found to exhibit a clear oscillation (beyond the uncertainty in measurement which is of the order of the size of the symbols), while there is no similar effect in the large-pore silica gel. We may imply that similarity in pore sizes and in the extension of the complexes formed by the interacting acetone and *n*-alkane molecules amplifies the effect of interaction oscillation. Thus, in complete agreement with the tendency observed with the oscillation of the melting points, even-numbered alkanes are found to give rise to a perceptibly smaller diffusivity, corresponding with larger complex sizes and, thus, stronger mutual interaction. That diffusion in the narrow-pore silica gel is found to be slowed down in comparison with diffusion in the large-pore sample in general, may be easily referred to an associated increase in tortuosity [55–58]. This effect is well known to increase with the size of the diffusing particle [59–61] which explains why the reduction in diffusivity in the narrow-pore silica gel is even more pronounced with acetone than with the *n*-alkanes (since, in contrast to acetone, only a minor part of the *n*-alkanes contributes to the complex formation).

3.3. Diffusion Studies with Nematic Liquid Crystals in Confining Pore Spaces

As considered in the previous section for neat liquids, pore space confinement is expected to also affect the internal dynamics in liquid crystals. As a rule, however, transverse nuclear magnetic relaxation in liquid crystals is known to be dramatically accelerated in comparison with the neat liquid [62,63], excluding the application of conventional PFG NMR for diffusion measurement. As an example of the application of MAS PFG NMR diffusion studies, Figure 6 shows a typical example of the MAS PFG NMR signal attenuation curves (Equation (6)) and an Arrhenius plot of the resulting diffusivities [21].

The measurements were performed with 4'-pentyl-4-cyanobiphenyl (5CB), a nematic liquid crystal commercially available (Merck Ltd., Poole, UK). The transition temperature between solid and the nematic phase is 297.2 K and the isotropization temperature is 308.5 K. Measurements were performed with both the bulk and with the liquid crystal confined within a Bioran porous glass with mean pore diameters of 30 nm and 200 nm. The data shown in Figure 6b are seen to comprise the diffusivities in both the states of nematic crystallinity (low temperatures) and isotropy (high temperatures). Sample heterogeneities and temperature variation over the sample (see Section 2) impeded sample equilibration for the temperatures in between so that in this range no measurements were performed.

While in the isotropic state, diffusivities are seen to decrease with increasing confinement, i.e., with the highest diffusivities in the bulk and with diffusivities in Bioran glasses with pore diameter of 30 nm below those measured for pore diameters of 200 nm, the effect of confinement is reversed in the nematic phase. Here, the diffusivities in the larger pores are seen to be below those in the smaller ones. This dependency reversal did already appear in Figure 6a where at 299 K, i.e., within the nematic phase, the decay of the attenuation curve (being proportional to the diffusivity—see Equation (6)) is seen to decrease with increasing pore size, while it increases at 334 K, i.e., in the isotropic state. A significant difference in the microdynamics of the two phases does as well appear in the activation energies of diffusion where, with (38 ± 6) kJ mol⁻¹, the value determined for the nematic phase notably exceeds that of (27 ± 5) kJ mol⁻¹ determined for the isotropic state. Simultaneously, the pre-exponential factor of the diffusivity in the nematic phase is seen to notably exceed that in the isotropic phase, following the correlation pattern of the compensation effect. Further enhancement in measurement accuracy is needed for a clear distinction between these two influences, promoting the elaboration of expedient model conceptions for explaining the observed diffusion anomalies.

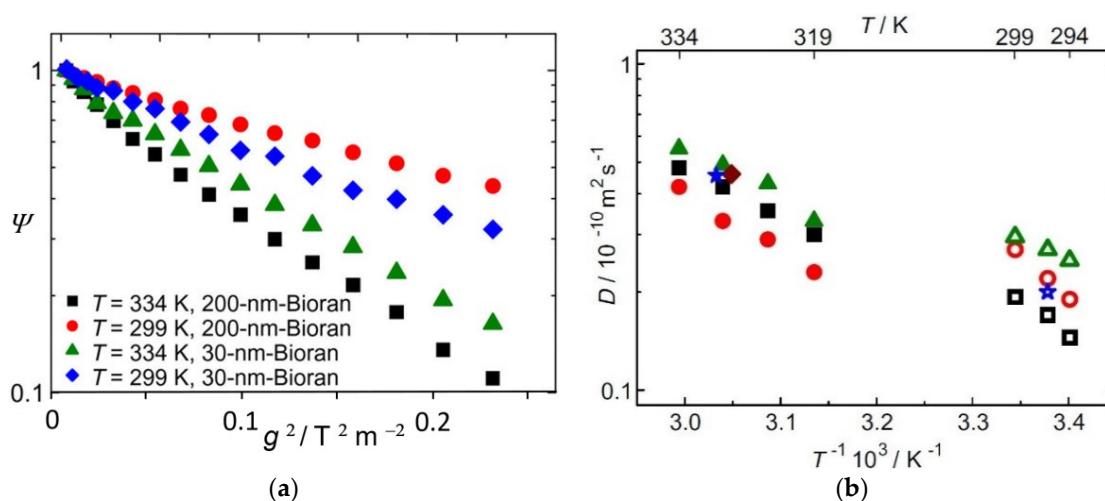


Figure 6. (a) ¹H MAS PFG NMR spin echo attenuation, ψ , of the 4'-pentyl-4-cyanobiphenyl (5CB) confined in Bioran glasses with pore diameters of 30 and 200 nm. (b) Temperature dependence of the diffusion coefficient D of bulk 5CB (\blacktriangle) and of 5CB confined in Bioran glasses with pore diameter of 30 nm (\bullet) and 200 nm (\blacksquare). The diffusivities were measured at 10 kHz rotation frequency, except three values for 200 nm Bioran glass, which were measured at 5 kHz (\star) and without rotation (\diamond). Empty symbols correspond to the nematic isotropic phase and full symbols correspond to the isotropic phase [21].

3.4. Water Diffusion in Lithium-Exchanged Low-Silica X-Type Zeolites

While in Sections 3.1 and 3.2, resolution enhancement by MAS PFG NMR was exploited for selective diffusion measurement of different components, it may also, equally importantly, be applied for studying the transport patterns of one and the same molecular species in different surroundings. Similarly as in micro-mesoporous hierarchical host materials [64–70] where guest molecules are known to propagate with different diffusion rates depending on their current position (i.e., within micro- or transport pores), overall mass transfer in complex systems is often found to occur in a sequence of subsequent displacements covered with different diffusion rates. First-order simulations of mass transfer in such systems are often based on the two-region approach of PFG NMR [71] where the diffusants are implied to diffuse at two different rates $D_{1,2}$, with the respective probabilities $p_{1,2}$ and the mean life times $\tau_{1,2}$ in either of these states [72–77]. Data analysis is significantly facilitated if the two states of mobility give rise to two different signals [14,78].

Figure 7 introduces a system where such a possibility could be exploited. It shows, on the right-hand side, the electron-microscopic picture of a low-silicon zeolite of type X (LSX) [79,80]. The individual particles are seen to be polycrystalline agglomerates. Diffusion studies by conventional PFG NMR have shown that the boundaries between the individual crystallites act as transport resistances for the water molecules, just as for the lithium cations whose diffusivities could, within these materials, be directly measured via PFG NMR for the very first time [81,82]. The schematics in the bottom of the left side show the zeolite pore structure, with the faujasite cage as the main storage place for the water molecules (accommodating about 30 water molecules) and the sodalite cage (with about 4 water molecules). Exchange between the various faujasite cages appears at an extremely fast rate (with mean lifetimes of the order of nanoseconds) while water in the sodalite cages remains kept over tens of milliseconds [81]. As an effect of its small exchange rates and, moreover, an extremely short transverse magnetic relaxation time, sodalite water does not contribute to the measurement of water diffusion by conventional PFG NMR measurements. Figure 8 illustrates that the situation becomes totally different under the conditions of MAS PFG NMR [83].

We do now note a clearly visible signal stemming also from the water kept within the sodalite units. It is well separated from a notably larger line which is caused by the water molecules in the large faujasite cages. These water molecules are, via the gas phase, in fast exchange within the whole bed of host particles. At a temperature of 313 K, water diffusion within the particles and through the bed is seen to give rise to a signal attenuation. Following the general relationship as provided by Equation (6), signal attenuation increases with increasing observation time. There is no signal attenuation visible for the sodalite water, in complete agreement with our understanding that the water molecules are kept caught within the individual sodalite cages.

At 373 K and for an observation time of 100 ms, signal attenuation is also observed with the water molecules contained in the sodalite cages. This indicates that now, at the increased temperature and for the largest observation time, at least a part of the water molecules within the sodalite cages have been replaced by molecules from the surroundings which, on their way through the sodalite cages and the intercrystalline space, have covered long-enough diffusion pathways giving rise to the observed attenuation.

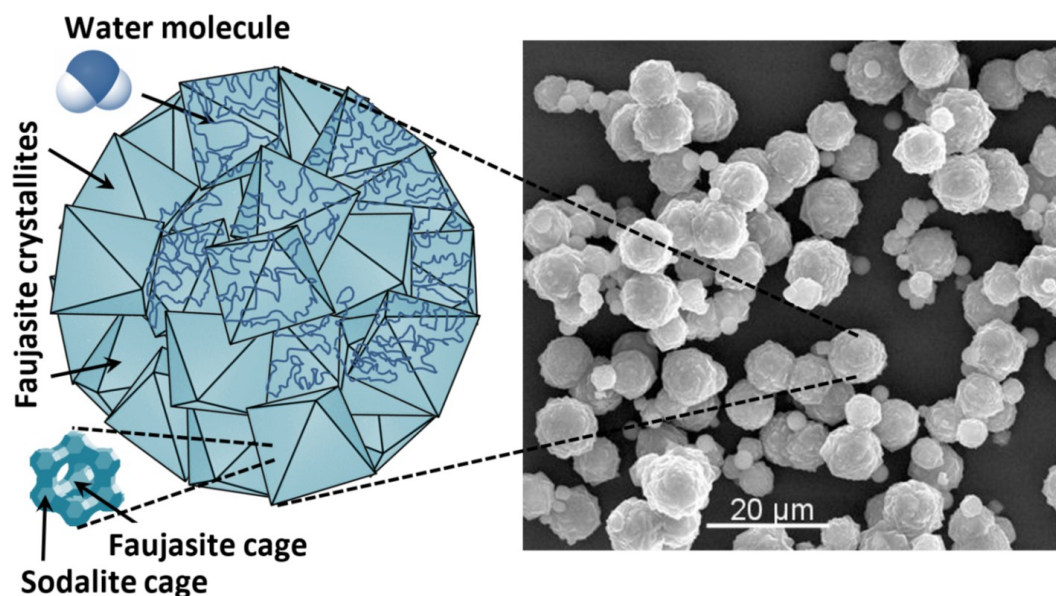


Figure 7. Electron microscopic picture of the LSX zeolite material under study (**right**) and schematics of the structure of the individual zeolite particles, jointly with a model of the pore elements, the “faujasite cage” surrounded by eight “sodalite cages”, with the latter ones acting as “traps” on the diffusion path of the water molecules (**left**). Figure 1 from Ref. [83] with permission.

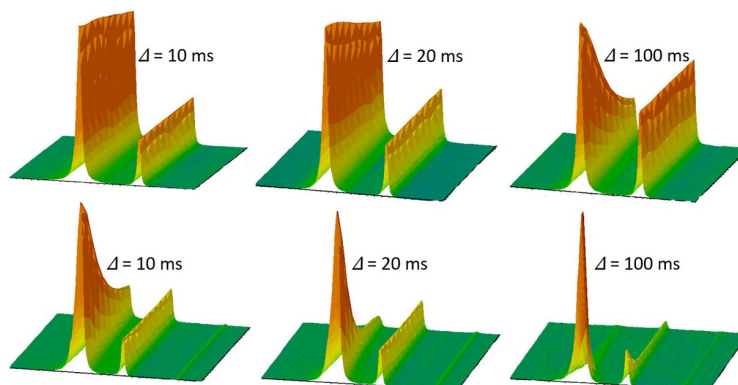


Figure 8. Stack plots of the ^1H MAS PFG NMR signal attenuation for water in 100Li-LSX at 313 K (top) and 373 K (bottom) for the indicated observation times. Chemical shifts increase from 7 ppm to 2 ppm (from left to right), and field gradient amplitudes from 0.011 T m^{-1} to 0.486 T m^{-1} . Figure 4 from Ref. [83] with permission.

Data analysis on the basis of the two-region model of PFG NMR diffusion measurement [14,71,78] yields, as a best fit to the experimentally determined attenuations shown in Figure 8, the dependencies of Figure 9 [83]. We note that this approach yields particularly satisfactory agreement for sodalite water whose mean lifetime within the sodalite cages at 373 K may thus be estimated to amount to 60 ms. Significant differences are observed between measurement and model approaches when considering the water molecules out of the sodalite cages. This may, however, be easily understood as an immediate consequence of the simplifications inherent to the model: while mass transfer outside of the sodalite cages is quite a complex phenomenon including molecular displacements both within the individual host particles and through interparticle space, additionally subject to resistances at the interface between the individual crystallites [82], in the two-region model of PFG NMR, all these influences are lumped together, being represented by one (“effective”) diffusivity.

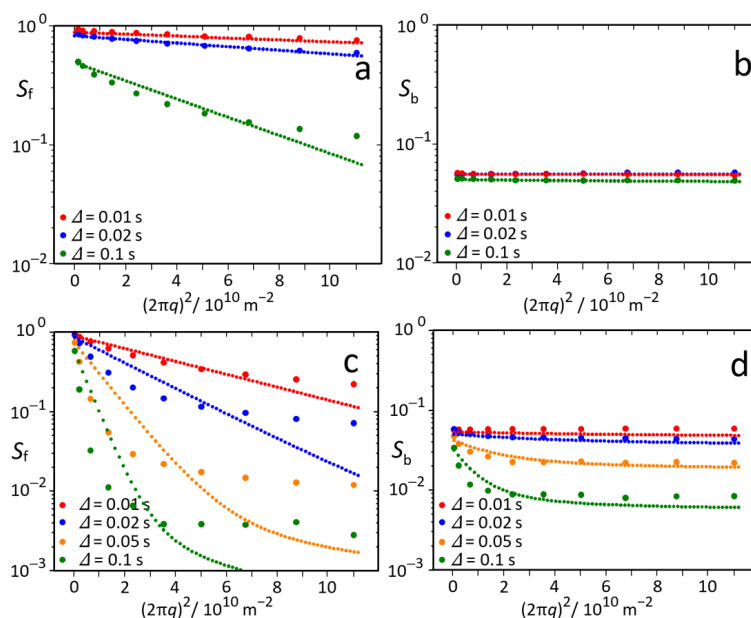


Figure 9. Intensity of the ^1H signal (balls) in MAS PFG NMR signal attenuation experiments for water molecules outside (left: (a,c)) and inside (right: (b,d)) the sodalite cages as a function of the (squared) field gradient pulse intensity in zeolite 100Li-LSX at 313 K (a,b) and 373 K (c,d) for different observation times Δ and comparison with the best fit (lines) as resulting from application of the two-region model. Figure 6 from Ref. [83] with permission.

3.5. Proton Mobility in Functionalized Mesoporous Materials

Increasing environmental pollution and ebbing away of conventional sources have given rise to steadily increasing efforts searching for alternative energy sources and for higher efficiencies in energy use. These activities include, in particular, the development and exploitation of novel fuel cell technologies. Performance improvements and quests for multifunctionality in application have led to increasingly complex structures, such as to be typically encountered with Polymer Electrolyte Membrane Fuel Cells [84–86]. Variety in charge carriers and the diffusion pathways covered by them make MAS PFG NMR a measuring technique of choice for an in-depth exploration of the elementary steps of charge carrier mass transfer in such systems.

For exemplifying the thus-attainable information, we refer to Figure 10. It shows the (highly resolved) proton spectra and their attenuation with increasing pulsed field gradient intensity for two functionalized siliceous materials. They are candidates for a composite fuel cell membrane consisting of a water-storing solid material and the common polymer material [87,88]. Both materials have been synthesized by co-condensation using tetraethylorthosilicate (TEOS) and mercaptopropyl-trimethoxysilane (MPMS) [87,88] and bear coinciding functional groups ($\equiv\text{Si}-\text{CH}_2-\text{CH}_2-\text{CH}_2-\text{SO}_3\text{H}$). They are linked to the siliceous host framework and possess an acidic hydrogen, representing the crucial “ingredient” for the use of such materials in fuel cells. The host particles of the specimens under study do, however, notably differ in size, which turns out to make, in the present context, the most relevant difference.

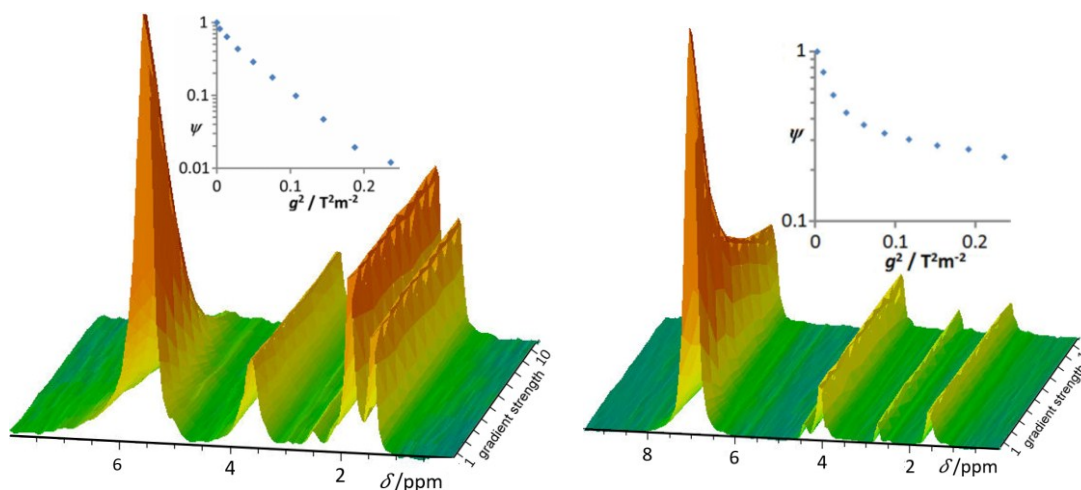


Figure 10. Two-dimensional presentations of the signal decay with linearly increasing strength of the gradient pulses and insets showing the semilogarithmic plot of the signal decay as a function of the squared strength of the gradient pulses. The ^1H MAS NMR experiments were performed at $100\text{ }^\circ\text{C}$. Results for sample MCM-48 and sample KIT-6 are presented on the left and right, respectively [88].

From the given material description, we easily recognize, in the various lines between 1 ppm and 4 ppm shown in Figure 10, the contribution of the protons in the CH_2 groups which remain unaffected by the field gradient pulses. The line at about 6 ppm, however, is clearly seen to be subject to signal attenuation by diffusion. It may be attributed, therefore (and also in total agreement with our knowledge about the chemical shift with protons in such systems [25,81,82,87,88]), to the acidic protons and to the protons of the water molecules within the host material, being in mutual fast exchange.

Quantitative analysis yields, for the signal attenuation (inserts in Figure 10) in the case of functionalized MCM-48, purely exponential decay as required by Equation (6), yielding a value of $1.9 \times 10^{-8}\text{ m}^2\text{ s}^{-2}$. Since the mean particle size of the MCM-48 material under study ($<0.1\text{ }\mu\text{m}$) is significantly exceeded by the mean diffusion path length considered in this study (about $34\text{ }\mu\text{m}$ for an observation time of 10 ms), the thus-attained diffusivities no longer reflect any features of

intracrystalline diffusion. They are rather given by the product of the relative number of molecules outside of the individual particles and their diffusivities. These “long-range” diffusivities are indeed known to be able to attain extremely large values, possibly even exceeding those in the liquid [89,90]. Estimates on the basis of the Nernst-Einstein equation by impedance spectroscopy (i.e., by conductivity measurements) for the identical system did correspondingly yield, with a value of $1.65 \times 10^{-11} \text{ m}^2 \text{ s}^{-2}$, notably smaller intracrystalline diffusivities [88].

Measurements with KIT-6 could be performed with notably larger host particles, with particle sizes up to 50 μm . Signal attenuation for the mobile protons is now found to be nicely approached by the superposition of two exponentials of the type of Equation (6). The fast decay is, once again, attributed to those water molecules which, during the observation time, have left their particles and could thus “benefit” from the high mobility in intercrystalline space. Their “effective” diffusivity amounts to $4.5 \times 10^{-9} \text{ m}^2 \text{ s}^{-2}$ which is, not unexpectedly, of a similar order of magnitude as already observed for long-range diffusion in MCM-48. Now, however, a substantial amount of the protons (water molecules) is seen to remain exclusively within the intraparticle pore space, giving rise to an intraparticle diffusivity of $2.3 \times 10^{-10} \text{ m}^2 \text{ s}^{-2}$. This value is indeed of the same order as the result of impedance spectroscopy which yielded a diffusivity of $3.04 \times 10^{-10} \text{ m}^2 \text{ s}^{-2}$ [88], in complete agreement with our understanding.

4. Conclusions

Experimental techniques are, by their very nature, only applicable to certain systems and under certain conditions. In the course of time, these limitations may become increasingly cumbersome—notably with powerful techniques, in view of their rich potential. As a consequence, further research work aiming at a release of these limitations is stimulated. It is often accompanied by an improvement of the performance and an enlargement of the applicability of these techniques, which have become possible based on these developments.

All these features may be recognized in following the introduction and further development of the pulsed field gradient (PFG) technique of NMR. Its application to studying molecular diffusion in complex media, notably in nanoporous host-guest systems, has provided us with a number of surprises, cumulating in a novel view on mass transfer in a number of nanoporous materials like zeolites in comparison with our understanding a couple of decades ago. In addition, this technique is subject to strict limitations, notably concerning the displacements of the molecules under study. Sensitivity towards displacements is—via transverse nuclear magnetic relaxation—particularly limited for systems of low mobility. Difficulties (with the measurement of displacements) are thus found to arise preferably in such cases where they are particularly harmful, namely with systems of particularly low mobility, with particularly low molecular shifts. In this mutual affectedness, one may recognize one of the versions of Murphy’s law.

A way out of this conflict is provided by combining magic-angle spinning (MAS) with PFG NMR diffusion measurement. The present review introduces the fundamentals of this approach and illustrates the novel potential with a number of cases. They include diffusion measurements with systems of extremely low mobility just as with multicomponent systems where, for the first time, diffusion coefficients of the various components have become accessible. MAS PFG NMR has thus contributed to a notable broadening of the scope so far considered in PFG NMR diffusion studies, including the investigation of fuel cells and of oscillations in the diffusion patterns of *n*-alkane–ketone mixtures under confinement. A most decisive breakthrough has been achieved in MAS PFG NMR diffusion studies with water in low-silicon lithium-exchanged zeolite X, where even water molecules confined to the sodalite cages have been made accessible to direct diffusion measurement. This type of measurement has all potential for becoming applicable to materials with hierarchically organized pore spaces in general, notably including mesoporous zeolites [56,91,92]. In-depth studies of molecular exchange between the various subspaces are among the great challenges of future investigations aiming

at quality enhancement and exploration of the elementary steps behind the overall performance of such materials.

Acknowledgments: We are grateful to all co-authors of our MAS PFG NMR studies which were presented in this review. Financial support by the German Science Foundation (HA 1893-16) and Fonds der Chemischen Industrie is gratefully acknowledged.

Conflicts of Interest: The authors declare no conflict of interest.

References

1. Bunde, A.; Caro, J.; Kärger, J.; Vogl, G. (Eds.) *Diffusive Spreading in Nature, Technology and Society*; Springer International Publishing: Cham, Switzerland, 2018.
2. Ruthven, D.M.; Farooq, S.; Knaebel, K.S. *Pressure Swing Adsorption*; VCH: New York, NY, USA, 1994.
3. Schüth, F.; Sing, K.S.W.; Weitkamp, J. (Eds.) *Handbook of Porous Solids*; Wiley-VCH: Weinheim, Germany, 2002.
4. Ertl, G.; Knözinger, H.; Schüth, F.; Weitkamp, J. (Eds.) *Handbook of Heterogeneous Catalysis*, 2nd ed.; Wiley-VCH: Weinheim, Germany, 2008.
5. Van de Voorde, M.H.; Sels, B. (Eds.) *Nanotechnology in Catalysis: Applications in the Chemical Industry, Energy Development, and Environment Protection*; Wiley-VCH: Weinheim, Germany, 2017.
6. Chen, N.Y.; Degnan, T.F.; Smith, C.M. *Molecular Transport and Reaction in Zeolites*; VCH: New York, NY, USA, 1994.
7. Kärger, J.; Freude, D. Mass transfer in micro- and mesoporous materials. *Chem. Eng. Technol.* **2002**, *25*, 769–778. [[CrossRef](#)]
8. Kärger, J.; Ruthven, D.M.; Theodorou, D.N. *Diffusion in Nanoporous Materials*; Wiley-VCH: Weinheim, Germany, 2012.
9. Kärger, J. Diffusionsuntersuchung von Wasser an 13X- sowie 4A- und 5A-Zeolithen mit Hilfe der Methode der gepulsten Feldgradienten. *Z. Phys. Chem.* **1971**, *248*, 27–41. [[CrossRef](#)]
10. Kärger, J.; Vasenkov, S. Quantitation of diffusion in zeolite catalysts. *Microporous Mesoporous Mater.* **2005**, *85*, 195–206. [[CrossRef](#)]
11. Valiullin, R. *Diffusion NMR of Confined Systems*; Royal Society of Chemistry: Cambridge, UK, 2016.
12. Kärger, J.; Heink, W. The Propagator Representation of Molecular Transport in Microporous Crystallites. *J. Magn. Reson.* **1983**, *51*, 1–7. [[CrossRef](#)]
13. Callaghan, P.T. *Principles of NMR Microscopy*; Clarendon Press: Oxford, UK, 1991.
14. Price, W.S. *NMR Studies of Translational Motion*; Cambridge University Press: Cambridge, UK, 2009.
15. Kärger, J. (Ed.) *Leipzig, Einstein, Diffusion*, 3rd ed.; Leipziger Universitätsverlag: Leipzig, Germany, 2014.
16. Zhdanov, S.P.; Khvostchov, S.S.; Feoktistova, N.N. *Synthetic Zeolites*; Gordon and Breach: New York, NY, USA, 1990.
17. Kärger, J. Measurement of diffusion in zeolites—A never ending challenge? *Adsorption* **2003**, *9*, 29–35. [[CrossRef](#)]
18. Gaede, H.C.; Gawrisch, K. Multi-dimensional pulsed field gradient magic angle spinning NMR experiments on membranes. *Magn. Reson. Chem.* **2004**, *42*, 115–122. [[CrossRef](#)] [[PubMed](#)]
19. Pampel, A.; Zick, K.; Glauner, H.; Engelke, F. Studying lateral diffusion in lipid bilayers by combining a magic angle spinning NMR probe with a microimaging gradient system. *J. Am. Chem. Soc.* **2004**, *126*, 9534–9535. [[CrossRef](#)] [[PubMed](#)]
20. Fernandez, M.; Kärger, J.; Freude, D.; Pampel, A.; van Baten, J.M.; Krishna, R. Mixture diffusion in zeolites studied by MAS PFG NMR and molecular simulation. *Microporous Mesoporous Mater.* **2007**, *105*, 124–131. [[CrossRef](#)]
21. Romanova, E.E.; Grinberg, F.; Pampel, A.; Kärger, J.; Freude, D. Diffusion studies in confined nematic liquid crystals by MAS PFG NMR. *J. Magn. Reson.* **2009**, *196*, 110–114. [[CrossRef](#)] [[PubMed](#)]
22. Gratz, M.; Hertel, S.; Wehring, M.; Stallmach, F.; Galvosas, P. Mixture diffusion of adsorbed organic compounds in metal-organic frameworks as studied by magic-angle spinning pulsed-field gradient nuclear magnetic resonance. *New J. Phys.* **2011**, *13*, 045016. [[CrossRef](#)]
23. Kimmich, R. *NMR Tomography, Diffusometry, Relaxometry*; Springer: Berlin, Germany, 1997.

24. Valiullin, R.; Kärger, J. Confined Fluids: NMR Perspectives on Confinements and on Fluid Dynamics. In *Diffusion NMR of Confined Systems*; Valiullin, R., Ed.; Royal Society of Chemistry: Cambridge, UK, 2016; pp. 390–434.
25. Harris, R.K.; Becker, E.D.; De Menezes, S.M.C.; Goodfellow, R.; Granger, P. NMR Nomenclature. Nuclear Spin Properties and Conventions for Chemical Shifts—(IUPAC Recommendations 2001). *Pure Appl. Chem.* **2001**, *73*, 1795–1818. [[CrossRef](#)]
26. Callaghan, P.T.; Coy, A.; MacGowan, D.; Packer, K.J.; Zelaya, F.O. Diffraction-like effects in NMR diffusion studies of fluids in porous solids. *Nature* **1991**, *351*, 467–469. [[CrossRef](#)]
27. Cussler, E.L. *Diffusion: Mass Transfer in Fluid Systems*, 3rd ed.; Cambridge University Press: Cambridge, UK, 2009.
28. Rousselot-Pailley, P.; Maux, D.; Wieruszkeski, J.M.; Aubagnac, J.L.; Martinez, J.; Lippens, G. Impurity detection in solid-phase organic chemistry: Scope and limits of HR MAS NMR. *Tetrahedron* **2000**, *56*, 5163–5167. [[CrossRef](#)]
29. Schröder, H. High resolution magic angle spinning NMR for analyzing small molecules attached to solid support. *J. Comb. Chem.* **2003**, *6*, 741–753. [[CrossRef](#)]
30. Pampel, A.; Fernandez, M.; Freude, D.; Kärger, J. New options for measuring molecular diffusion in zeolites by MAS PFG NMR. *Chem. Phys. Lett.* **2005**, *407*, 53–57. [[CrossRef](#)]
31. Schlayer, S.; Stallmach, F.; Horch, C.; Splith, T.; Pusch, A.-K.; Pielenz, F.; Peksa, M. Konstruktion und Test eines Gradientensystems für NMR-Diffusionsuntersuchungen in Grenzflächensystemen. *Chem. Ing. Tech.* **2013**, *85*, 1755–1760. [[CrossRef](#)]
32. Romanova, E.E.; Scheffler, F.; Freude, D. Crystallization of zeolite MFI under supergravity, studied in situ by 11B MAS NMR spectroscopy. *Microporous Mesoporous Mater.* **2009**, *126*, 268–271. [[CrossRef](#)]
33. Dvoyashkina, N.; Freude, D.; Stepanov, A.G.; Böhlmann, W.; Krishna, R.; Kärger, J.; Haase, J. Alkane/alkene mixture diffusion in silicalite-1 studied by MAS PFG NMR. *Microporous Mesoporous Mater.* **2018**, *257*, 128–134. [[CrossRef](#)]
34. Mildner, T.; Ernst, H.; Freude, D. 207Pb NMR detection of spinning-induced temperature gradients in MAS rotors. *Solid State Nucl. Magn. Reson.* **1995**, *5*, 269–271. [[CrossRef](#)]
35. Ferguson, D.B.; Haw, J.F. Transient methods for in-situ NMR of reactions on solid catalysts using temperature jumps. *Anal. Chem.* **1995**, *67*, 3342–3348. [[CrossRef](#)]
36. Neue, G.; Dybowski, C. Determining temperature in a magic-angle spinning probe using the temperature dependence of the isotropic chemical shift of lead nitrate. *Solid State Nucl. Magn. Reson.* **1997**, *7*, 333–336. [[CrossRef](#)]
37. Chmelik, C.; Freude, D.; Bux, H.; Haase, J. Ethane/ethene mixture diffusion in the MOF sieve ZIF-8 studied by MAS PFG NMR diffusometry. *Microporous Mesoporous Mater.* **2012**, *147*, 135–141. [[CrossRef](#)]
38. Chmelik, C. Characteristic features of molecular transport in MOF ZIF-8 as revealed by IR microimaging. *Microporous Mesoporous Mater.* **2015**, *216*, 138–145. [[CrossRef](#)]
39. Park, K.S.; Ni, Z.; Cote, A.P.; Choi, J.Y.; Huang, R.D.; Uribe-Romo, F.J.; Chae, H.K.; O’Keeffe, M.; Yaghi, O.M. Exceptional chemical and thermal stability of zeolitic imidazolate frameworks. *Proc. Natl. Acad. Sci. USA* **2006**, *103*, 10186–10191. [[CrossRef](#)] [[PubMed](#)]
40. Bux, H.; Liang, F.; Li, Y.; Cravillon, J.; Wiebcke, M.; Caro, J. Zeolitic imidazolate framework membrane with molecular sieving properties by microwave-assisted solvothermal synthesis. *J. Am. Chem. Soc.* **2009**, *131*, 16000–16001. [[CrossRef](#)] [[PubMed](#)]
41. Lu, G.; Hupp, J.T. Metal-organic frameworks as sensors: A ZIF-8 based Fabry-Pérot device as a selective sensor for chemical vapors and gases. *J. Am. Chem. Soc.* **2010**, *132*, 7832–7833. [[CrossRef](#)] [[PubMed](#)]
42. Kärger, J.; Binder, T.; Chmelik, C.; Hibbe, F.; Krautscheid, H.; Krishna, R.; Weitkamp, J. Microimaging of transient guest profiles to monitor mass transfer in nanoporous materials. *Nat. Mater.* **2014**, *13*, 333–343. [[CrossRef](#)] [[PubMed](#)]
43. Gladstone, S.; Laidler, K.J.; Eyring, H. *The Theory of Rate Processes*; McGraw-Hill: New York, NY, USA, 1941.
44. Ruthven, D.M.; Derrah, R.I. Transition state theory of zeolitic diffusion. *J. Chem. Soc. Faraday Trans. I* **1972**, *68*, 2332–2343. [[CrossRef](#)]
45. Kärger, J.; Pfeifer, H.; Haberlandt, R. Application of absolute rate theory to intracrystalline diffusion in zeolites. *J. Chem. Soc. Faraday Trans. I* **1980**, *76*, 1569–1575. [[CrossRef](#)]

46. Chmelik, C.; Kärger, J. The predictive power of classical transition state theory revealed in diffusion studies with MOF ZIF-8. *Microporous Mesoporous Mater.* **2016**, *225*, 128–132. [[CrossRef](#)]
47. Caro, J.; Bülow, M.; Schirmer, W.; Kärger, J.; Heink, W.; Pfeifer, H.; Zhdanov, S.P. Microdynamics of methane, ethane and propane in ZSM-5 type zeolites. *J. Chem. Soc. Faraday Trans. I* **1985**, *81*, 2541–2550. [[CrossRef](#)]
48. Heink, W.; Kärger, J.; Pfeifer, H.; Salverda, P.; Datema, K.P.; Nowak, A.K. High-temperature pulsed field gradient nuclear magnetic resonance self-diffusion measurements of n-Alkanes in MFI-type zeolites. *J. Chem. Soc. Faraday Trans.* **1992**, *88*, 3505–3509. [[CrossRef](#)]
49. Jobic, H.; Schmidt, W.; Krause, C.; Kärger, J. PFG NMR and QENS diffusion studies of n-alkane homologues in MFI-type zeolites. *Microporous Mesoporous Mater.* **2006**, *90*, 299–306. [[CrossRef](#)]
50. Tsai, H.L.; Sato, S.; Takahashi, R.; Sodesawa, T.; Takenaka, S. Liquid-phase hydrogenation of ketones in the mesopores of nickel catalysts. *Phys. Chem. Chem. Phys.* **2002**, *4*, 3537–3542. [[CrossRef](#)]
51. Nguyen, N.Q.; McGann, M.R.; Lacks, D.J. Elastic stability limits of polyethylene and n-alkane crystals from molecular simulation. *J. Phys. Chem. B* **1999**, *103*, 10679–10683. [[CrossRef](#)]
52. Kishore, K.; Bharat, S.; Kannan, S. Correlation of Kauzmann temperature with odd-even effect in n-alkanes. *J. Chem. Phys.* **1996**, *105*, 11364–11365. [[CrossRef](#)]
53. Takahashi, R.; Sato, S.; Sodesawa, T.; Ikeda, T. Diffusion coefficient of ketones in liquid media within mesopores. *Phys. Chem. Chem. Phys.* **2003**, *5*, 2476–2480. [[CrossRef](#)]
54. Fernandez, M.; Pampel, A.; Takahashi, R.; Sato, S.; Freude, D.; Kärger, J. Revealing complex-formation in acetone-n-alkane mixtures by MAS PFG NMR diffusion measurement in nanoporous hosts. *Phys. Chem. Chem. Phys.* **2008**, *10*, 4165–4171. [[CrossRef](#)] [[PubMed](#)]
55. Rincon Bonilla, M.; Bhatia, S.K. Diffusion in Pore Networks: Effective self-diffusivity and the concept of tortuosity. *J. Phys. Chem. C* **2013**, *117*, 3343–3357. [[CrossRef](#)]
56. Rincon Bonilla, M.; Titze, T.; Schmidt, F.; Mehlhorn, D.; Chmelik, C.; Valiullin, R.; Bhatia, S.K.; Kaskel, S.; Ryoo, R.; Kärger, J. Diffusion study by IR micro-imaging of molecular uptake and release on mesoporous zeolites of structure type CHA and LTA. *Materials* **2013**, *6*, 2662–2688. [[CrossRef](#)] [[PubMed](#)]
57. Kärger, J.; Valiullin, R. Mass transfer in mesoporous materials: The benefit of microscopic diffusion measurement. *Chem. Soc. Rev.* **2013**, *42*, 4172–4197. [[CrossRef](#)] [[PubMed](#)]
58. Mehlhorn, D.; Kondrashova, D.; Küster, C.; Enke, D.; Emmerich, T.; Bunde, A.; Valiullin, R.; Kärger, J. Diffusion in complementary pore spaces. *Adsorption* **2016**, *22*, 879–890. [[CrossRef](#)]
59. Stoeckel, D.; Kübel, C.; Hormann, K.; Hölzel, A.; Smarsly, B.M.; Tallarek, U. Morphological analysis of disordered macroporous-mesoporous solids based on physical reconstruction by nanoscale tomography. *Langmuir* **2014**, *30*, 9022–9027. [[CrossRef](#)] [[PubMed](#)]
60. Kondrashova, D.; Lauerer, A.; Mehlhorn, D.; Jobic, H.; Feldhoff, A.; Thommes, M.; Chakraborty, D.; Gommers, C.; Zecevic, J.; de Jongh, P.; et al. Scale-dependent diffusion anisotropy in nanoporous silicon. *Sci. Rep.* **2017**, *7*, 40207. [[CrossRef](#)] [[PubMed](#)]
61. Reich, S.-J.; Svidrytski, A.; Hölzel, A.; Florek, J.; Kleitz, F.; Wang, W.; Kübel, C.; Hlushkou, D.; Tallarek, U. Hindered diffusion in ordered mesoporous silicas: Insights from pore-scale simulations in physical reconstructions of SBA-15 and KIT-6 silica. *J. Phys. Chem. C* **2018**, *122*, 12350–12361. [[CrossRef](#)]
62. Crawford, G.P.; Vilfan, M.; Doane, J.W.; Vilfan, I. Escaped-radial nematic configuration in submicrometer-size cylindrical cavities: Deuterium nuclear-magnetic-resonance study. *Phys. Rev. A* **1991**, *43*, 835–842. [[CrossRef](#)] [[PubMed](#)]
63. Cramer, C.; Cramer, T.; Arndt, M.; Kremer, F.; Naji, L.; Stannarius, R. NMR and dielectric studies of nano-confined nematic liquid crystals. *Mol. Cryst. Liq. Cryst. Sci. Technol. Sect. A Mol. Cryst. Liq. Cryst.* **2006**, *303*, 209–217. [[CrossRef](#)]
64. Gueudré, L.; Milina, M.; Mitchell, S.; Pérez-Ramírez, J. Superior mass transfer properties of technical zeolite bodies with hierarchical porosity. *Adv. Funct. Mater.* **2014**, *24*, 209–219. [[CrossRef](#)]
65. Mitchell, S.; Pinar, A.B.; Kenvin, J.; Crivelli, P.; Kärger, J.; Pérez-Ramírez, J. Structural analysis of hierarchically organized zeolites. *Nat. Commun.* **2015**, *6*, 8633. [[CrossRef](#)] [[PubMed](#)]
66. Hartmann, M.; Schwieger, W. Hierarchically-structured porous materials: From basic understanding to applications. *Chem. Soc. Rev.* **2016**, *45*, 3311–3312. [[CrossRef](#)] [[PubMed](#)]
67. Coasne, B. Multiscale adsorption and transport in hierarchical porous materials. *New J. Chem.* **2016**, *40*, 4078–4094. [[CrossRef](#)]

68. Galarneau, A.; Guenneau, F.; Gedeon, A.; Mereib, D.; Rodriguez, J.; Fajula, F.; Coasne, B. Probing interconnectivity in hierarchical microporous/mesoporous materials using adsorption and nuclear magnetic resonance diffusion. *J. Phys. Chem. C* **2016**, *120*, 1562–1569. [[CrossRef](#)]
69. Trogadas, P.; Nigra, M.M.; Coppens, M.-O. Nature-inspired optimization of hierarchical porous media for catalytic and separation processes. *New J. Chem.* **2016**, *40*, 4016–4026. [[CrossRef](#)]
70. Coppens, M.O.; Ye, G. Nature-inspired optimization of transport in porous media. In *Diffusive Spreading in Nature, Technology and Society*; Bunde, A., Caro, J., Kärger, J., Vogl, G., Eds.; Springer International Publishing: Cham, Switzerland, 2018; pp. 203–232.
71. Kärger, J. NMR Self-diffusion studies in heterogeneous systems. *Adv. Colloid Interface Sci.* **1985**, *23*, 129–148. [[CrossRef](#)]
72. Reginald Waldeck, A.; Hossein Nouri-Sorkhabi, M.; Sullivan, D.R.; Kuchel, P.W. Effects of cholesterol on transmembrane water diffusion in human erythrocytes measured using pulsed field gradient NMR. *Biophys. Chem.* **1995**, *55*, 197–208. [[CrossRef](#)]
73. Meier, C.; Dreher, W.; Leibfritz, D. Diffusion in compartmental systems. II. Diffusion weighted measurements of rat brain tissue in vivo and postmortem at very large b -values. *Magn. Reson. Med.* **2003**, *50*, 510–514. [[CrossRef](#)] [[PubMed](#)]
74. Nilsson, M.; Alerstam, E.; Wirestam, R.; Stahlberg, F.; Brockstedt, S.; Lätt, J. Evaluating the accuracy and precision of a two-compartment Kärger model using Monte Carlo simulations. *J. Magn. Res.* **2010**, *206*, 59–67. [[CrossRef](#)] [[PubMed](#)]
75. Himmelein, S.; Sporenberg, N.; Schönhoff, M.; Ravoo, B.J. Size-selective permeation of water-soluble polymers through the bilayer membrane of cyclodextrin vesicles investigated by PFG-NMR. *Langmuir* **2014**, *30*, 3988–3995. [[CrossRef](#)] [[PubMed](#)]
76. Melchior, J.-P.; Majer, G.; Kreuer, K.-D. Why do proton conducting polybenzimidazole phosphoric acid membranes perform well in high-temperature PEM fuel cells? *Phys. Chem. Chem. Phys.* **2016**, *19*, 601–612. [[CrossRef](#)] [[PubMed](#)]
77. Ferreira, A.S.D.; Barreiros, S.; Cabrita, E.J. Probing sol-gel matrices microenvironments by PGSE HR-MAS NMR. *Magn. Reson. Chem.* **2017**, *55*, 452–463. [[CrossRef](#)] [[PubMed](#)]
78. Cabrita, E.J.; Berger, S.; Brauer, P.; Kärger, J. High-resolution DOSY NMR with spins in different chemical surroundings: Influence of particle exchange. *J. Magn. Reson.* **2002**, *157*, 124–131. [[CrossRef](#)] [[PubMed](#)]
79. Kühl, G.H. Crystallization of low-silica faujasite. *Zeolites* **1987**, *7*, 451–457. [[CrossRef](#)]
80. Schneider, D.; Toufar, H.; Samoson, A.; Freude, D. ^{17}O DOR and other solid-state NMR studies concerning the basic properties of zeolites LSX. *Solid State Nucl. Magn. Reson.* **2009**, *35*, 87–92. [[CrossRef](#)] [[PubMed](#)]
81. Freude, D.; Beckert, S.; Stallmach, F.; Kurzhals, R.; Täschner, D.; Toufar, H.; Kärger, J.; Haase, J. Ion and water mobility in hydrated Li-LSX zeolite studied by ^1H , ^6Li and ^7Li NMR spectroscopy and diffusometry. *Microporous Mesoporous Mater.* **2013**, *172*, 174–181. [[CrossRef](#)]
82. Beckert, S.; Stallmach, F.; Toufar, H.; Freude, D.; Kärger, J.; Haase, J. Tracing water and cation diffusion in hydrated zeolites of type Li-LSX by pulsed field gradient NMR. *J. Phys. Chem. C* **2013**, *117*, 24866–24872. [[CrossRef](#)]
83. Lauerer, A.; Kurzhals, R.; Toufar, H.; Freude, D.; Kärger, J. Tracing compartment exchange by NMR diffusometry: Water in lithium-exchanged low-silica X zeolites. *J. Magn. Reson.* **2018**, *289*, 1–11. [[CrossRef](#)] [[PubMed](#)]
84. Laberty-Robert, C.; Vallé, K.; Pereira, F.; Sanchez, C. Design and properties of functional hybrid organic-inorganic membranes for fuel cells. *Chem. Soc. Rev.* **2011**, *40*, 961–1005. [[CrossRef](#)] [[PubMed](#)]
85. Hickner, M.A.; Ghassemi, H.; Kim, Y.S.; Einsla, B.R.; McGrath, J.E. Alternative polymer systems for proton exchange membranes (PEMs). *Chem. Rev.* **2004**, *104*, 4587–4612. [[CrossRef](#)] [[PubMed](#)]
86. Kreuer, K.-D.; Paddison, S.J.; Spohr, E.; Schuster, M. Transport in proton conductors for fuel-cell applications: simulations, elementary reactions, and phenomenology. *Chem. Rev.* **2004**, *104*, 4637–4678. [[CrossRef](#)] [[PubMed](#)]
87. Sharifi, M.; Wark, M.; Freude, D.; Haase, J. Highly proton conducting sulfonic acid functionalized mesoporous materials studied by impedance spectroscopy, MAS NMR spectroscopy and MAS PFG NMR diffusometry. *Microporous Mesoporous Mater.* **2012**, *156*, 80–89. [[CrossRef](#)]

88. Dvoyashkina, N.; Seidler, C.F.; Wark, M.; Freude, D.; Haase, J. Proton mobility in sulfonic acid functionalized mesoporous materials studied by MAS PFG NMR diffusometry and impedance spectroscopy. *Microporous Mesoporous Mater.* **2018**, *255*, 140–147. [[CrossRef](#)]
89. D’Orazio, F.; Bhattacharja, S.; Halperin, W.P.; Gerhardt, R. Enhanced self-diffusion of water in restricted geometry. *Phys. Rev. Lett.* **1989**, *63*, 43–46. [[CrossRef](#)] [[PubMed](#)]
90. Kärger, J.; Pfeifer, H.; Riedel, E.; Winkler, H. Self-diffusion measurements of water adsorbed in NaY zeolites by means of NMR pulsed field gradient techniques. *J. Colloid Interface Sci.* **1973**, *44*, 187–188. [[CrossRef](#)]
91. Inayat, A.; Knoke, I.; Spieker, E.; Schwieger, W. Assemblies of mesoporous FAU-type zeolite nanosheets. *Angew. Chem. Int. Ed.* **2012**, *51*, 1962–1965. [[CrossRef](#)] [[PubMed](#)]
92. Na, K.; Choi, M.; Ryoo, R. Recent advances in the synthesis of hierarchically nanoporous zeolites. *Microporous Mesoporous Mater.* **2013**, *166*, 3–19. [[CrossRef](#)]



© 2018 by the authors. Licensee MDPI, Basel, Switzerland. This article is an open access article distributed under the terms and conditions of the Creative Commons Attribution (CC BY) license (<http://creativecommons.org/licenses/by/4.0/>).